CENTRE FOR **STOCHASTIC GEOMETRY**
AND ADVANCED **BIOIMAGING**

Sabrina Tang Christensen and Markus Kiderlen

Comparison of two global digital algorithms for Minkowski tensor estimation

No. 10, July 2016

Comparison of two global digital algorithms for Minkowski tensor estimation

Sabrina Tang Christensen and Markus Kiderlen

Department of Mathematics, Aarhus University

Abstract

The geometry of real world objects can be described by Minkowski tensors. Algorithms have been suggested to approximate Minkowski tensors if only a binary image of the object is available. This paper presents implementations of two such algorithms. The theoretical convergence properties are confirmed by simulations on test sets, and recommendations for input arguments of the algorithms are given. For increasing resolutions, we obtain more accurate estimators for the Minkowski tensors. Digitisations of more complicated objects are shown to require higher resolutions.

Keywords: Minkowski tensor; digital algorithm; set with positive reach; digitisation

1 Introduction

Image analysis is the interpretation of discrete representations of real world objects. Its wide range of applications can be found in fields such as Biology [2, 5], Physics [10], and Materials Sciences [18, 19]. Traditional digital geometry [11] uses binary information to assess volume or surface area or, more generally, intrinsic volumes of (sufficiently regular) sets $A \subset \mathbb{R}^n$. More recently, the estimation of Minkowski tensors has been suggested, as tensor-valued valuations allow for quantification of location- and orientation-related properties of A.

In [8], algorithms for the estimation of Minkowski tensors of sets with positive reach from digitisations are introduced. The derivation of the algorithms is based on a generalised Steiner formula, and the estimators can be shown to converge to the true tensors as the resolution d of the digitisation tends to infinity. This property is called multigrid convergence, and the results on multigrid convergence of the estimators are presented as Theorems 3.1 and 4.1 of this paper.

We have implemented two of the algorithms described in [8] in MATLAB. In dimension n and for a set $A \subset \mathbb{R}^n$ with $\operatorname{Reach}(A) > 0$, one algorithm depends on the choice of $n+1$ radii $0 < R_0 < \cdots < R_n < \operatorname{Reach}(A)$; the other on n radii $0 < R_0 < \cdots < R_{n-1} < \operatorname{Reach}(A)$. We have implemented the algorithms in MATLAB in dimension $n = 2$. Based on simulations for both convex and non-convex

test sets with positive reach via our digital algorithms, we will give recommendations for the choices of the radii on which the algorithms are based. Further, we explore the consequences of making erroneous choices of the radii, i.e. choosing them larger than $\operatorname{Reach}(A)$. We also discuss a possible lower limit $d/\sqrt{2}$ for the radii. Finally, both algorithms are multigrid convergent, and we wish to explore how well the theory carries over when the algorithms are applied in the realistic setting of finite resolution.

In Section 2, we introduce the notions of *positive reach* and *digitisation*, and we give the definition of *Minkowski tensors*. Section 3 presents the first algorithm and its implementation as well as a review of the method for obtaining the estimators via a generalised Steiner formula. In Section 4 follows the second algorithm and corresponding implementation. Having established the algorithms, we proceed to perform simulations on test sets in Section 5 and examine the theoretical properties of the algorithms in applications. In Section 6 we give recommendations for the choices of input arguments for the algorithms based on our findings in Section 5.

2 Preliminaries

We equip Euclidean n-space $\mathbb{R}^n$ with the standard inner product $\langle \cdot, \cdot \rangle$ and induced norm $|\cdot|$. For a compact set $A \subset \mathbb{R}^n$, let $d_A(x)$ be the distance of $x \in \mathbb{R}^n$ to A and write

$$A^R = \{x \in \mathbb{R}^n \mid d_A(x) \leq R\}$$

for the ***R*-parallel set** of A, $R \geq 0$. Denote by $\operatorname{Unp}(A) \subset \mathbb{R}^n$ the set of all points $x \in \mathbb{R}^n$ which have a unique nearest point in A and by $\operatorname{Exo}(A) \subset \mathbb{R}^n$ the complement of $\operatorname{Unp}(A)$ in $\mathbb{R}^n$; the **exoskeleton** of A. Note that x belongs to the exoskeleton of A if and only if the closed ball $B_R(x)$ with radius $R = d_A(x)$ and centre x has more than one point of intersection with A. Let $p_A \colon \operatorname{Unp}(A) \to A$ be the metric projection which maps a point $x \in \operatorname{Unp}(A)$ to its unique nearest point $p_A(x)$ in A. If $A^R \cap \operatorname{Exo}(A) = \emptyset$, all points at distance at most R from A have a unique nearest point in A, i.e. $A^R \subset \operatorname{Unp}(A)$. If R' is the supremum of all R such that this property holds, A is said to have **reach** R'. When R' is positive, A is called a **set with positive reach**. By Motzkin's theorem, see for instance [16, Theorem 1.2.4], a set has infinite reach if and only if it is convex. Another example of sets with positive reach are ρ-regular sets introduced independently by Pavlidis [15, Definition 7.4] and Serra [20, Definition p. 144] and often used in digital geometry due to their favourable properties under digitisation; see for instance [4] and [21]. A set $A \subset \mathbb{R}^n$ is called ρ-regular if both A and the closure of its complement A^C have reach at least ρ.

2.1 Digitisations

Letting $\mathbb{Z}$ denote the integers, a cubic lattice $dL \subset \mathbb{R}^n$ is any rotated, translated version of $d\mathbb{Z}^n \subset \mathbb{R}^n$, where $d > 0$ is called the **lattice distance**. An element $l \in dL$ is called a **sampling point**. We adopt a basic digitisation model of a set $A \subset \mathbb{R}^n$

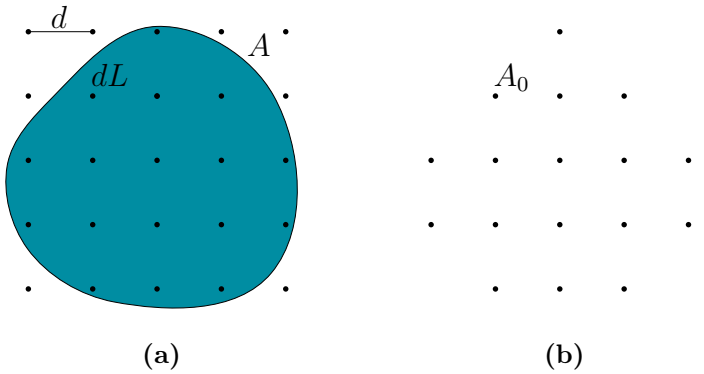

Figure 1: Illustration of the digitisation process in dimension 2. The compact set $A \subset \mathbb{R}^2$ (blue) in (a) is digitised to $A_0 = A \cap dL$ in (b).

by considering the set

$$A_0 = A \cap dL$$

of all lattice points in A. In signal processing, A_0 is interpreted as the result of an ideal sampler. The discrete set A_0 is called the **digitisation** of A by dL, and d^{-1} is called the **resolution** of the digitisation. Figure 1 illustrates the digitisation process.

The **Voronoi cell** of $x \in A_0$ with respect to the digitisation A_0 is defined as

$$\begin{aligned}\mathcal{V}_{A_0}(x) &= \{y \in \mathbb{R}^n \mid |y - x| \leq |y - z| \text{ for all } z \in A_0\} \\ &= \mathrm{cl}\{y \in \mathrm{Unp}(A_0) \mid p_{A_0}(y) = x\},\end{aligned}$$

where $\mathrm{cl}(X)$ denotes the closure of a set $X \subset \mathbb{R}^n$. A Voronoi cell of a sampling point $x \in A_0$ is called a Voronoi cell of A_0. The Voronoi cells of A_0 have pairwise disjoint interiors, and their (finite) union coincides with $\mathbb{R}^n$. Similarly, we may choose to consider Voronoi cells with respect to a lattice dL (a locally finite set),

$$\mathcal{V}_{dL}(x) = \mathrm{cl}\{y \in \mathrm{Unp}(dL) \mid p_{dL}(y) = x\},$$

where $x \in dL$. The set $\mathcal{V}_{dL}(x)$ is an n-dimensional hypercube in $\mathbb{R}^n$ with side length d and centre x. In $\mathbb{R}^2$, $\mathcal{V}_{dL}(x)$ can be interpreted as the **pixel** of x.

Clearly $\mathcal{V}_{A_0}(x)$ is a hypercube of side length d if and only if the $2n$ neighbours of x in the axis directions of dL are all elements of A_0. In this case $\mathcal{V}_{A_0}(x) = \mathcal{V}_{dL}(x)$, and we say that x is an **inner point** of A_0. In the plane, x is an inner point if its usual four-neighbours are in A_0; see Figure 2 for an illustration.

In this paper, we work exclusively with binary representations of the underlying set $A \subset \mathbb{R}^n$. Colouring $\mathcal{V}_{dL}(x)$ black whenever $x \in A_0$ and white otherwise, A_0 can be represented as a black-and-white digital image, the so-called Gauss-digitisation [11] of A. Given the lattice dL, the Gauss-digitisation and A_0 capture the same information of the underlying set A. Therefore, all the results for A_0 that follow can equivalently be formulated using the Gauss-digitisation.

2.2 Minkowski tensors

One purpose of image processing is the extraction of geometric characteristics of an object from a digital image. We give here a short introduction to a rather general

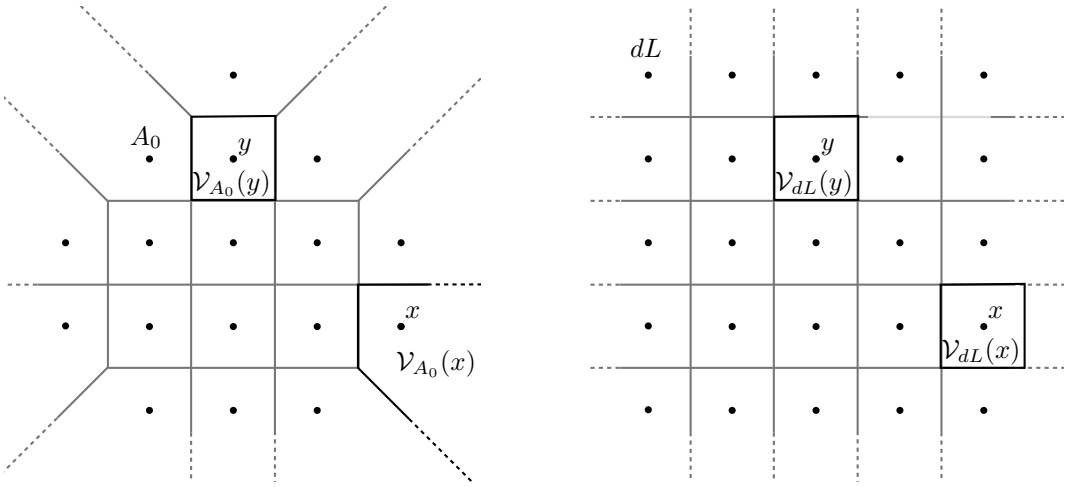

Figure 2: Comparison of Voronoi cells with respect to a digitisation $A_0 \subset dL$ in (a) and with respect to a lattice dL in (b). Here y is an inner point of A_0 whereas x is not.

class of such characteristics; the so-called Minkowski tensors. For a more thorough review, the reader may consult the excellent book [16] by Schneider.

For $p \in \mathbb{N}_0$, let $\mathbb{T}^p$ denote the space of symmetric tensors of rank p on $\mathbb{R}^n$. Using the scalar product to identify $\mathbb{R}^n$ with its dual, an element T of $\mathbb{T}^p$ defines a symmetric p-linear functional $T\colon (\mathbb{R}^n)^p \to \mathbb{R}$. Any $T \in \mathbb{T}^p$ is determined by the numbers

$$T_{(i_1 \dots i_p)} = T(e_{i_1}, \dots, e_{i_p}), \tag{2.1}$$

$i_1, \dots, i_p \in \{1, \dots, n\}$, where $e_1, \dots, e_n$ is the standard basis in $\mathbb{R}^n$. In particular, a tensor of rank zero, one, and two can be identified with a scalar, a vector in $\mathbb{R}^n$, and a symmetric matrix of size $n \times n$, respectively. More generally, a tensor of rank p can be identified with a symmetric array of size n^p. When calculating tensors later on, it will be the entries of this array that we calculate.

Denote by x^r the r-fold tensor product of $x \in \mathbb{R}^n$, which is given by

$$x^r(v_1, \dots, v_r) = \prod_{i=1}^{r} \langle x, v_i \rangle, \qquad v_1, \dots, v_r \in \mathbb{R}^n,$$

and by ab the symmetric tensor product of symmetric tensors a and b. We use the convention that $x^0 = 1$.

For a compact subset A of $\mathbb{R}^n$, we define an element of $\mathbb{T}^r$, called the ***r*'th volume tensor** of A, by

$$\Phi_n^{r,0}(A) = \frac{1}{r!} \int_A x^r \mathrm{d}x. \tag{2.2}$$

Notice in particular that $\Phi_n^{0,0}(A)$ is simply the volume $V_n(A)$ of A. For $s \geq 1$, we put $\Phi_n^{r,s}(A) = 0$. More general tensors related to A can be defined by integrating over boundary points and outer normal vectors when A is a set with positive reach.

Let $A \subset \mathbb{R}^n$ be a set with positive reach. For $k = 0, 1, \dots, n-1$ and $r, s \in \mathbb{N}_0$, we define elements of $\mathbb{T}^{r+s}$ by

$$\Phi_k^{r,s}(A) = \frac{1}{r!s!} \frac{\omega_{n-k}}{\omega_{n-k+s}} \int_{\mathbb{R}^n \times S^{n-1}} x^r u^s \Lambda_k(A; \mathrm{d}(x, u)), \tag{2.3}$$

where S^{j-1} is the unit sphere in $\mathbb{R}^j$, ω_j is the surface area of S^{j-1}, and $\Lambda_k(A;\cdot)$ is the generalised curvature measure of A introduced in [23]. For all $k = 0, 1, \ldots, n$ and $r,\ s \geq 0$, $\Phi_k^{r,s}(A)$ are the **Minkowski tensors** of A. For $r = s = 0$, the Minkowski tensors $\Phi_k^{0,0}(A)$, $k = 0, 1, \ldots, n$, coincide with the *k'th intrinsic volumes* $V_k(A)$ of A; see for instance [16], as was already noted in the case of the volume $V_n(A)$. In particular, $2V_{n-1}(A)$ is the surface area of A when A does not have lower dimensional parts, and $V_0(A)$ is the Euler-Poincaré characteristic of A. By restricting the integrations in (2.2) and (2.3) to $B \cap A$ respectively $B \times S^{n-1}$ with $B \subset \mathbb{R}^n$ a Borel set, local Minkowski tensors can be defined as suggested in [7]. Although the digital algorithms for estimating Minkowski tensors are formulated using the local versions, we restrict our considerations to the estimation of Minkowski tensors of the form (2.2) and (2.3).

3 Minkowski tensor estimation from $n+1$ parallel sets

Steiner's formula, in its version for sets $A \subset \mathbb{R}^n$ with positive reach, shows that the parallel volume $V_n(A^R)$ is a polynomial in R of degree at most n as long as $0 \leq R < \mathrm{Reach}(A)$. Up to constants, its coefficients are coinciding with the intrinsic volumes $V_0(A), \ldots, V_n(A)$. This allows for the computation (estimation) of the intrinsic volumes when $V_n(A^R)$ is (approximately) known for different radii R. Replacing the parallel volume with the Voronoi tensors measures, to be defined below, this idea can be extended to an estimation procedure for Minkowski tensors.

3.1 The Voronoi tensor measures

For a compact set $A \subset \mathbb{R}^n$ and $R \geq 0$, the formula

$$\mathcal{V}_R^{r,s}(A) = \int_{A^R} p_A(x)^r (x - p_A(x))^s \mathrm{d}x \tag{3.1}$$

defines $\mathbb{T}^{r+s}$-valued measures $\mathcal{V}_R^{r,s}(A)$. These are called the (total) **Voronoi tensor measures** and were first introduced by Hug, Kiderlen, and Svane in [8]. In the case where A has positive reach, $0 \leq R < \mathrm{Reach}(A)$, a Steiner-type formula implies that

$$\mathcal{V}_R^{r,s}(A) = r!s! \sum_{k=0}^{n} \kappa_{s+k} R^{s+k} \Phi_{n-k}^{r,s}(A), \tag{3.2}$$

where κ_j is the volume of the unit ball in $\mathbb{R}^j$.

For $n+1$ different choices of R, $0 < R_0 < R_1 < \cdots < R_n < \mathrm{Reach}(A)$, equation (3.2) gives rise to a system of $n+1$ linear equations for each pair (r, s);

$$\begin{pmatrix} \mathcal{V}_{R_0}^{r,s}(A) \\ \vdots \\ \mathcal{V}_{R_n}^{r,s}(A) \end{pmatrix} = M_{R_0,\ldots,R_n}^{r,s} \begin{pmatrix} \Phi_n^{r,s}(A) \\ \vdots \\ \Phi_0^{r,s}(A) \end{pmatrix}, \tag{3.3}$$

with the matrix

$$M^{r,s}_{R_0,\dots,R_n} = r!s! \begin{pmatrix} \kappa_s R_0^s & \dots & \kappa_{s+n} R_0^{s+n} \\ \vdots & \ddots & \vdots \\ \kappa_s R_n^s & \dots & \kappa_{s+n} R_n^{s+n} \end{pmatrix}.$$

The matrix $M^{r,s}_{R_0,\dots,R_n}$ is a Vandermonde-type matrix and so in particular invertible, hence (3.3) can be solved for the Minkowski tensors;

$$\begin{pmatrix} \Phi^{r,s}_n(A) \\ \vdots \\ \Phi^{r,s}_0(A) \end{pmatrix} = \left(M^{r,s}_{R_0,\dots,R_n}\right)^{-1} \begin{pmatrix} \mathcal{V}^{r,s}_{R_0}(A) \\ \vdots \\ \mathcal{V}^{r,s}_{R_n}(A) \end{pmatrix}. \tag{3.4}$$

We wish to utilise (3.4) for the estimation of Minkowski tensors from digitisations. To this end, suitable estimators for the Voronoi tensor measures on the right-hand side of (3.4) must be introduced.

3.2 Estimators for Minkowski tensors from digitisations

Let dL be a lattice. Given a digitisation $A_0 = A \cap dL$ of a set $A \subset \mathbb{R}^n$ with positive reach, $\operatorname{Reach}(A) > R \geq 0$, we approximate the Voronoi tensor measure $\mathcal{V}^{r,s}_R(A)$ by the corresponding quantity $\mathcal{V}^{r,s}_R(A_0)$ for A_0. This yields estimators

$$\begin{pmatrix} \hat{\Phi}^{r,s}_n(A_0) \\ \vdots \\ \hat{\Phi}^{r,s}_0(A_0) \end{pmatrix} = \left(M^{r,s}_{R_0,\dots,R_n}\right)^{-1} \begin{pmatrix} \mathcal{V}^{r,s}_{R_0}(A_0) \\ \vdots \\ \mathcal{V}^{r,s}_{R_n}(A_0) \end{pmatrix} \tag{3.5}$$

for the Minkowski tensors; compare (3.4). The justification for replacing $\mathcal{V}^{r,s}_R(A)$ with its discrete counterpart $\mathcal{V}^{r,s}_R(A_0)$ is given in [8, Theorem 4.3], which implies that $\mathcal{V}^{r,s}_R(A_0)$ converges to $\mathcal{V}^{r,s}_R(A)$ as $d \to 0^+$ under weak assumptions on A. This yields the following convergence theorem result for $\hat{\Phi}^{r,s}_R(A)$ when A is topologically regular, that is, A is the closure of its interior. This seems a reasonable restriction when working with digitisations, since the lower dimensional parts of an object are generally not visible in the digital image A_0.

Theorem 3.1 *Let $A \subset \mathbb{R}^n$ be compact and topologically regular. If $\hat{\Phi}^{r,s}_k(A \cap dL)$ is defined by equation (3.5) with $A_0 = A \cap dL$ and $0 < R_0 < \dots < R_n < \operatorname{Reach}(A)$, then $\hat{\Phi}^{r,s}_k(A \cap dL)$ is **multigrid convergent** to $\Phi^{r,s}_k(A)$, which means*

$$\lim_{d \to 0^+} \hat{\Phi}^{r,s}_k(A \cap dL) = \Phi^{r,s}_k(A). \tag{3.6}$$

A proof of Theorem 3.1 can be found in [8, Corollary 5.2]. If, in addition, A is convex or ρ-regular, the convergence in (3.6) is of order $O(d)$ when $r = s = 0$, that is, for estimators of the intrinsic volumes. For $(r, s) \neq (0, 0)$, convergence is known to be of order $O(\sqrt{d})$.

Equation (3.5) gives a set of estimators for all the Minkowski tensors, but alternative estimators exist in the case of the volume tensors given by (2.2). We will return to these considerations in Section 4, where we introduce an additional algorithm which exploits this fact. For now, we can use (3.5) to compute estimators for

the Minkowski tensors of a set $A \subset \mathbb{R}^n$ with positive reach from a digitisation A_0. In the next subsection, we will explain how the Voronoi tensor measures can be computed for discrete sets.

3.3 Implementation in dimension two

For $x \in A_0$, we have the relation $\mathcal{V}_{A_0}(x) \cap A_0^R = \mathcal{V}_{A_0}(x) \cap B_R(x)$, and we will refer to this intersection as the ***R*-bounded Voronoi cell** of $x \in A_0$ with respect to A_0. The space $\mathbb{R}^n$ coincides with the finite union of the Voronoi cells of A_0, so A_0^R coincides with the union of R-bounded Voronoi cells of A_0. This yields a simplification of (3.1) for the discrete set A_0,

$$\mathcal{V}_R^{r,s}(A_0) = \sum_{x \in A_0} x^r \int_{\mathcal{V}_{A_0}(x) \cap B_R(x)} (y-x)^s \mathrm{d}y. \tag{3.7}$$

Thus, the Voronoi tensor measures for discrete digitisations can be reduced to a sum of contributions from each element of A_0, and these contributions depend only on the corresponding R-bounded Voronoi cells of A_0. The right-hand side of equation (3.5) is now easily computed using (3.7). This will be our first algorithm.

We choose to focus on dimension two for the implementation of the algorithm given by (3.5). In this case, (3.5) becomes

$$\begin{pmatrix} \hat{\Phi}_2^{r,s}(A_0) \\ \hat{\Phi}_1^{r,s}(A_0) \\ \hat{\Phi}_0^{r,s}(A_0) \end{pmatrix} = \left(M_{R_0,R_1,R_2}^{r,s}\right)^{-1} \begin{pmatrix} \mathcal{V}_{R_0}^{r,s}(A_0) \\ \mathcal{V}_{R_1}^{r,s}(A_0) \\ \mathcal{V}_{R_2}^{r,s}(A_0) \end{pmatrix} \tag{3.8}$$

with

$$M_{R_0,R_1,R_2}^{r,s} = r!s! \begin{pmatrix} \kappa_s R_0^s & \kappa_{s+1} R_0^{s+1} & \kappa_{s+2} R_0^{s+2} \\ \kappa_s R_1^s & \kappa_{s+1} R_1^{s+1} & \kappa_{s+2} R_1^{s+2} \\ \kappa_s R_2^s & \kappa_{s+1} R_2^{s+1} & \kappa_{s+2} R_2^{s+2} \end{pmatrix}.$$

In practice, one is usually interested in the tensors of rank at most two, i.e. tensors for which $r + s \leq 2$. The relevant volumes κ_j of the unit ball in $\mathbb{R}^j$ are thus

$$\kappa_0 = 1, \qquad \kappa_1 = 2, \qquad \kappa_2 = \pi, \qquad \kappa_3 = 4\pi/3, \qquad \kappa_4 = \pi^2/2. \tag{3.9}$$

From [16, (4.27),(5.18),(5.30)], it follows that for $k = 0, \ldots, n-1$, the tensor $\Phi_k^{0,1}(A) = 0$ is trivial. It is therefore not necessary to use approximations $\hat{\Phi}_k^{r,s}(A)$ in these cases. Nonetheless, our implementation calculates and reports these estimators, since values deviating considerably from the origin indicate that the resolution is not sufficiently high.

For a given digitisation A_0 of a set $A \subset \mathbb{R}^2$, the algorithm determines $\hat{\Phi}_k^{r,s}(A_0)$ by (3.7) and (3.8) based on three fixed radii $0 < R_0 < R_1 < R_2 < \mathrm{Reach}(A)$. The assumption that all radii must be smaller than $\mathrm{Reach}(A)$ requires the knowledge of (a positive lower bound of) the reach of A. Since the reach may not be accessible in applications, we also analyse the behaviour of the estimators when one or more radii are larger than $\mathrm{Reach}(A)$ in the simulation section.

The asymptotic result in Theorem 3.1 is based on increasing resolution ($d \to 0^+$). Hence any given radius $R > 0$ is eventually larger than half the diameter $d\sqrt{2}$ of

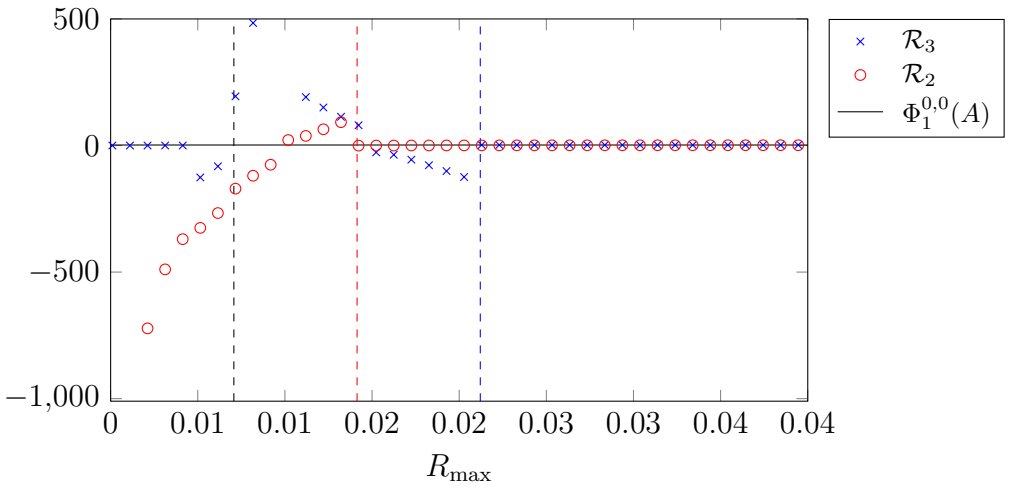

Figure 3: The estimators $\hat{\Phi}_1^{0,0}(A)$ and $\tilde{\Phi}_1^{0,0}(A)$ as functions of $R_{\max}$ for fixed resolution $d^{-1} = 100$ and different radii for the square $A = [0,1]^2$ with $R_0 = R_{\max}/n$ for $\mathcal{R}_n$, $n = 2, 3$. Here $\mathcal{R}_3$ denotes the algorithm presented in Section 3.3, $\mathcal{R}_2$ denotes the second algorithm to be introduced in Section 4, and $R_{\max}$ denotes the maximal radius R_{n-1} for $\mathcal{R}_n$. The third radius, R_1, of $\mathcal{R}_3$ is given by $R_1 = (R_0 + R_2)/2$. The second algorithm, $\mathcal{R}_2$, only depends on two radii. The dashed black line indicates the point when $R_{\max}$ is greater than $d/\sqrt{2}$; the coloured dashed lines when all radii of the corresponding algorithm are above $d/\sqrt{2}$.

a pixel, implying that the union of all R-bounded Voronoi cells of points $x \in A_0$ covers the Gauss-digitisation of A completely. On the other hand, if $R < d/\sqrt{2}$ for some $d > 0$, the R-bounded Voronoi cell of an inner point does not cover its pixel. In this case the replacement of $\mathcal{V}_R^{r,s}(A)$ by $\mathcal{V}_R^{r,s}(A_0)$ in the transition from (3.4) to (3.5) may cause unwanted errors. In fact, Figure 3 shows the behaviour of half the perimeter estimator $\hat{V}_1(A) = \hat{\Phi}_1^{0,0}(A)$ for the unit square $A = [0,1]^2$ when the radii vary in the vicinity of $d/\sqrt{2}$. The figure clearly illustrates the described effect. This effect can be avoided by choosing $R_0 > d/\sqrt{2}$, and we shall do so for the remainder of this paper.

As $R > d/\sqrt{2}$, one can simplify the computations in the algorithm in the following way. Under this assumption, the R_i-bounded Voronoi cell $\mathcal{V}_{A_0}(x) \cap B_{R_i}(x)$ of an inner point $x \in A_0$ coincides with $\mathcal{V}_{dL}(x)$. Hence the contributions of all inner points of the digitisation to the integral $\int_{\mathcal{V}_{A_0}(x)\cap B_{R_i}(x)} (y-x)^s \mathrm{d}y$ are the same and vanish when s is odd. This observation is exploited in the implementation of the algorithm in order to reduce computation times.

With the aforementioned choices, we obtain the following algorithm, where we restrict attention to estimators of Minkowski tensors of rank at most two. These tensors have been shown to be most relevant in practical applications such as those suggested at the beginning of the introduction. An extension to higher rank tensors is straightforward and only requires minor modifications in the code.

Algorithm Minktensor2D3R ($\mathcal{R}_3$)

Input:

- Digitisation $A_0 = A \cap dL$ of a compact topologically regular set $A \subset \mathbb{R}^2$ with positive reach;
- Lattice distance $d > 0$ of dL;
- Two radii R_0 and R_2 satisfying $0 < R_0 < R_2 < \mathrm{Reach}(A)$.

Action:

- Calculate $\mathcal{V}_{R_i}^{r,s}(A_0)$ using (3.7) for R_i, $i = 0, 1, 2$, with $R_1 = (R_0 + R_2)/2$, and for all $r, s \in \{0, 1, 2\}$ with $r + s \leq 2$;
- Determine the corresponding Minkowski tensors by (3.8).

Output:

- Estimators $\hat{\Phi}_k^{r,s}(A_0)$ for all $k, r, s \in \{0, 1, 2\}$ with $r + s \leq 2$ (including the trivial ones of the form $\hat{\Phi}_k^{0,1}(A_0)$ for model control) of the corresponding Minkowski tensors.

The programme will give a warning if radii are chosen below the recommended lower limit $d/\sqrt{2}$ as discussed above. If any result of the algorithm is numerically below 10^{-6}, the output is rounded off to zero.

4 Minkowski tensor estimation from n parallel sets

As proved in [8], it is possible to refine the algorithm introduced in Section 3.2 by using simpler estimators for the volume tensors defined in (2.2). Since we require that the set $A \subset \mathbb{R}^n$ be compact and topologically regular, one can use the estimators

$$\tilde{\Phi}_n^{r,0}(A_0) = \frac{d^n}{r!} \sum_{x \in A_0} x^r \tag{4.1}$$

for the volume tensors. This is the natural generalisation of the usual volume estimator in the case $r = 0$, which counts foreground pixels; see for instance [14]. Letting ∂A denote the boundary of A, we have the following result on convergence from [8, Section 5.1].

Theorem 4.1 *Let $A \subset \mathbb{R}^n$ be compact and topologically regular, and suppose ∂A is a Lebesgue null set. Then $\tilde{\Phi}_n^{r,0}(A \cap dL)$, defined by equation (4.1) with $A_0 = A \cap dL$, is multigrid convergent to $\Phi_n^{r,0}(A)$, i.e.*

$$\lim_{d \to 0^+} \tilde{\Phi}_n^{r,0}(A \cap dL) = \Phi_n^{r,0}(A). \tag{4.2}$$

The assumption that ∂A is a Lebesgue null set is weaker than that of positive reach, so these estimators converge towards the true volume tensors for a larger class of sets than $\hat{\Phi}_n^{r,0}$ do. Moreover, they do not require any knowledge of the reach of A. If, in addition, ∂A is an $(n-1)$-rectifiable set, i.e. if ∂A is the image of a bounded

subset of $\mathbb{R}^{n-1}$ under a Lipschitz map, the convergence in (4.2) is of order $O(d)$. This condition is for instance satisfied by ρ-regular sets.

In addition to their advantageous convergence properties, using the estimators in (4.1) for the volume tensors, we can derive an alternative algorithm for computation of estimators for the Minkowski tensors of sets A with positive reach, which is based on only n fixed radii $0 < R_0 < \cdots < R_{n-1} < \operatorname{Reach}(A)$.

Indeed, let $0 \leq R < \operatorname{Reach}(A)$ and consider the Voronoi tensor measures $\mathcal{V}_R^{r,s}(A)$ defined by (3.2). Subtract $r!s!\kappa_s R^s \Phi_n^{r,s}(A)$ from both sides of the equation to obtain

$$\mathcal{V}_R^{r,s}(A) - r!s!\kappa_s R^s \Phi_n^{r,s}(A) = r!s! \sum_{k=1}^{n} \kappa_{s+k} R^{s+k} \Phi_{n-k}^{r,s}(A). \tag{4.3}$$

In the case $s > 0$, $\Phi_n^{r,s}(A) = 0$, so (4.3) takes the simple form

$$\mathcal{V}_R^{r,s}(A) = r!s! \sum_{k=1}^{n} \kappa_{s+k} R^{s+k} \Phi_{n-k}^{r,s}(A), \quad s > 0, \tag{4.4}$$

and when $s = 0$,

$$\mathcal{V}_R^{r,0}(A) - r!\Phi_n^{r,0}(A) = r! \sum_{k=1}^{n} \kappa_k R^k \Phi_{n-k}^{r,0}(A). \tag{4.5}$$

Similarly to the approach used in section 3.1, estimators for the Minkowski tensors are obtained from (3.7), (4.4), and (4.5):

$$\begin{pmatrix} \tilde{\Phi}_{n-1}^{r,s}(A_0) \\ \vdots \\ \tilde{\Phi}_0^{r,s}(A_0) \end{pmatrix} = \left(N_{R_0,\ldots,R_{n-1}}^{r,s}\right)^{-1} \begin{pmatrix} \mathcal{V}_{R_0}^{r,s}(A_0) - r!\tilde{\Phi}_n^{r,s}(A_0) \\ \vdots \\ \mathcal{V}_{R_{n-1}}^{r,s}(A_0) - r!\tilde{\Phi}_n^{r,s}(A_0) \end{pmatrix} \tag{4.6}$$

for all $r, s \geq 0$, where a new Vandermonde-type matrix

$$N_{R_0,\ldots,R_{n-1}}^{r,s} = r!s! \begin{pmatrix} \kappa_{s+1} R_0^{s+1} & \ldots & \kappa_{s+n} R_0^{s+n} \\ \vdots & \ddots & \vdots \\ \kappa_{s+1} R_{n-1}^{s+1} & \ldots & \kappa_{s+n} R_{n-1}^{s+n} \end{pmatrix}$$

is introduced. The number of equations in the linear system described by (4.6) is reduced by one compared to (3.5). Once more, we note that for $s > 0$, $\Phi_n^{r,s}(A)$ equals 0 and can thus be estimated by $\tilde{\Phi}_n^{r,s}(A) = 0$, so the terms $r!\tilde{\Phi}_n^{r,s}(A_0)$ are put equal to zero.

It follows from Theorems 3.1 and 4.1 that $\tilde{\Phi}_k^{r,s}(A_0)$ is multigrid convergent for all $k = 0, \ldots, n$ and $r, s \in \mathbb{N}_0$ if A is compact and topologically regular and $0 < R_0 < \cdots < R_{n-1} < \operatorname{Reach}(A)$. A combination of [8, Theorem 4.2 and Lemma 5.1] and the remarks following Theorem 4.1 implies that this convergence is of order $O(d)$ when A is convex or ρ-regular and $r = s = 0$. For $(r, s) \neq (0, 0)$, the speed of convergence is $O(\sqrt{d})$.

Again, this algorithm has been implemented in the planar case. For $n = 2$, the algorithm in (4.6) reduces to

$$\begin{pmatrix} \tilde{\Phi}_1^{r,s}(A_0) \\ \tilde{\Phi}_0^{r,s}(A_0) \end{pmatrix} = \left(N_{R_0,R_1}^{r,s}\right)^{-1} \begin{pmatrix} \mathcal{V}_{R_0}^{r,s}(A_0) - r!\tilde{\Phi}_2^{r,s}(A_0) \\ \mathcal{V}_{R_1}^{r,s}(A_0) - r!\tilde{\Phi}_2^{r,s}(A_0) \end{pmatrix} \tag{4.7}$$

for $r, s \geq 0$, where $\tilde{\Phi}_2^{r,0}(A_0) = (d^2/r!) \sum_{x \in A_0} x^r$ and $N_{R_0,R_1}^{r,s}$ is defined as

$$N_{R_0,R_1}^{r,s} = r!s! \begin{pmatrix} \kappa_{s+1} R_0^{s+1} & \kappa_{s+2} R_0^{s+2} \\ \kappa_{s+1} R_1^{s+1} & \kappa_{s+2} R_1^{s+2} \end{pmatrix}$$

with κ_j given by (3.9).

Algorithm Minktensor2D2R ($\mathcal{R}_2$)

Input:

- Digitisation $A_0 = A \cap dL$ of a compact topologically regular set $A \subset \mathbb{R}^2$ with positive reach;
- Lattice distance $d > 0$ of dL;
- Two radii R_0 and R_1 satisfying $d/\sqrt{2} < R_0 < R_1 < \mathrm{Reach}(A)$.

Action:

- Calculate $\tilde{\Phi}_2^{r,0}(A_0)$ using (4.1) for $r \in \{0, 1, 2\}$;
- Calculate $\mathcal{V}_{R_i}^{r,s}(A_0)$ using (3.7) for R_1, R_2 and all $r, s \in \{0, 1, 2\}$ with $r + s \leq 2$;
- Determine the corresponding Minkowski tensors by (4.7).

Output:

- Estimators $\tilde{\Phi}_k^{r,s}(A_0)$ for all $k, r, s \in \{0, 1, 2\}$ with $r + s \leq 2$ (including the trivial ones of the form $\hat{\Phi}_k^{0,1}(A_0)$ for model control) of the corresponding Minkowski tensors.

The programme will give a warning if radii are chosen below the recommended lower limit $d/\sqrt{2}$ as discussed above. If any result of the algorithm is numerically below 10^{-6}, the output is rounded off to zero.

5 Simulations

In the preceding sections, we have introduced two different algorithms for the computation of estimators for the Minkowski tensors of sets $A \subset \mathbb{R}^2$ with positive reach from a digitisation $A_0 = A \cap dL$. We denote by $\mathcal{R}_3$ the first algorithm, introduced in Section 3, which is based on three radii $0 < R_0 \leq R_1 \leq R_2 < \mathrm{Reach}(A)$, and by $\mathcal{R}_2$ the second algorithm, introduced in Section 4, based on two radii $0 < R_0 \leq R_1 < \mathrm{Reach}(A)$. Theorems 3.1 and 4.1 on multigrid convergence of the algorithms do not depend on the specific choice of the radii, but we expect the choice to affect the accuracy at least to some extent: We have already argued that choosing radii below $d/\sqrt{2}$ is problematic, so we will impose the restriction $d/\sqrt{2} < R_0$ henceforth. Finally, we wish to explore the consequences of choosing one or more radii larger than $\mathrm{Reach}(A)$.

For $\mathcal{R}_3$, three Voronoi tensor measures $\mathcal{V}_{R_i}(A_0)$, $i = 0, 1, 2$, must be calculated and a system of three linear equations must be solved. For $\mathcal{R}_2$, only two Voronoi tensor measures $\mathcal{V}_{R_i}(A_0)$, $i = 1, 2$, are calculated and a system of two linear equations solved. As a trade-off, we must calculate estimators for the volume tensors $\Phi_2^{r,0}(A)$,

but these are computed quite effectively using the algorithm in (4.1). In particular, note that for the volume tensors, we need only compute the sum $\sum_{x\in A_0} x^r$ once for each r, the relevant values being $r \in \{0,1,2\}$, resulting in three simple computations. For the Voronoi tensor measures, computed via (3.7), we need computations for each choice of $r \in \{0,1,2\}$, for each choice of $s \geq 0$ such that $r+s \leq 2$, and for each choice of R_i. For $\mathcal{R}_3$ and hence three radii, this gives twelve computations; for $\mathcal{R}_2$ only nine. Hence the second algorithm requires fewer computations, and in particular, the number of computations of the more complicated integral on the right-hand side of (3.7), which depends on the Voronoi diagram, is reduced by three. We would thus expect $\mathcal{R}_2$ to be faster than $\mathcal{R}_3$ as the size of the data set A_0 increases or, equivalently, as the resolution grows.

5.1 Choices of radii

The purpose of this section is to give recommendations for proper choices of radii based on simulations with test sets. Let $R_{\max}$ be the maximal radius equal to R_2 in the case of $\mathcal{R}_3$ and to R_1 in the case of $\mathcal{R}_2$. To evaluate the behaviour of the estimators for varying choices of radii, the following procedure is used.

Procedure $\mathcal{P}$ for selecting radii

(1) For some fixed resolution, consider the interval $(d/\sqrt{2}, m)$ where $3d/\sqrt{2} < m < \mathrm{Reach}(A)$. Put $R_{\max} = m$ and $R_0 = R_{\max}/n$ for algorithm $\mathcal{R}_n$, $n = 2, 3$. This way, the radii are evenly spaced over the interval $(0, m)$ and all greater than $d/\sqrt{2}$. We now let m vary and plot the estimators of the Minkowski tensors as functions of m.

(2) Based on our findings in (1) and applying the same resolution, we choose a maximal radius in the interval $(d/\sqrt{2}, \mathrm{Reach}(A))$ for which we get satisfactory estimators in the previous simulations. We then choose R_0 in the interval $(d/\sqrt{2}, R_{\max})$. We plot the estimators as functions of R_0.

(3) Based on our findings in (2) and applying the same resolution, we choose a minimal radius $R_0 > d/\sqrt{2}$ for which we get satisfactory estimators in the previous simulations. We then choose $R_{\max}$ in the interval (R_0, m) where $m > R_0$. We plot the estimators as functions of $R_{\max}$.

If A is convex, there is no upper constraint on m or $R_{\max}$ in the above procedure. The procedure requires some choice of resolution. For the simulations below, we choose resolution $d^{-1} = 1000$.

We now apply procedure $\mathcal{P}$ to different test sets in $\mathbb{R}^2$. As test sets we have chosen, with increasing geometric complexity, a convex disc, a non-convex annulus, and a realisation of the complement of a planar Boolean model; see Figure 4.

Our starting point is the simple case of a translated unit disc $A = B_1 + (1,1)^T$, where we put $B_r = B_r(0)$, $r \geq 0$. We apply procedure $\mathcal{P}$ to A to find suitable radii for each of the algorithms; see Figure 5. In this figure, we only report results for the tensors $\Phi_k^{r,s}(A)$, $r, s \geq 0$, $r+s \leq 2$, in the case $k = 1$. The corresponding results for $k = 0$ are qualitatively the same. The case $k = 2$ stands out in that $\mathcal{R}_2$ makes use of

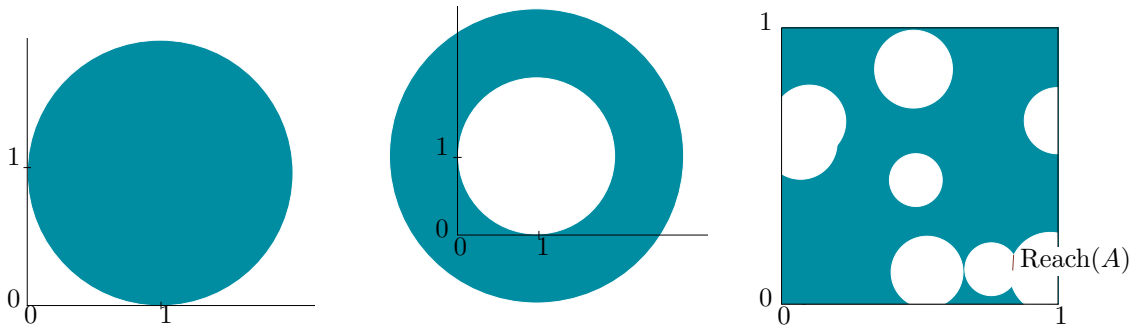

Figure 4: The three test sets used in our simulations. (a) shows the disc $B_1 + (1,1)^T$, (b) the annulus $\mathrm{cl}(B_2 \setminus B_1) + (1,1)^T$, and (c) the complement of one realisation of a Boolean model with intensity $\gamma = 10$ and uniform radius distribution $U(0.08, 0.16)$ for the typical particle.

(4.1) for the estimation of the volume tensors, and this formula does not depend on the radii. The results for the tensors with $k = 2$ are, however, very similar to those with $k \in \{0, 1\}$ for the algorithm $\mathcal{R}_3$, but to illustrate the difference in behaviour of $\mathcal{R}_2$, Figure 6 shows the results of step (1) of procedure $\mathcal{P}$ for volume tensors.

To report results, we use the identification of rank p tensors with the entries of the array of size n^p as explained in (2.1). As there are 12 non-trivial components of tensors $\Phi_1^{r,s}(A)$ with $r, s \geq 0$, $r + s \leq 2$, we only report a selection of such entries. To concretise, $\Phi_1^{0,0}(A) = \pi$ is half the perimeter of A , and $\Phi_1^{1,0}(A)$ is, up to normalisation, the centre of gravity of a uniform mass distribution on ∂A. Hence $\Phi_1^{1,0}(A)_{(1)}$ is the projection of this centre of gravity onto the x-axis. Another example is

$$\Phi_1^{2,0}(A) = \frac{1}{2} \int_{\partial A} x^2 \mathcal{H}^1(\mathrm{d}x),$$

where $\mathcal{H}^1$ denotes the one-dimensional Hausdorff measure. Hence

$$\Phi_1^{2,0}(A)_{(i,j)} = \frac{1}{2} \int_{\partial A} x_i x_j \mathcal{H}^1(\mathrm{d}x).$$

In particular, for Figures 5(b) and (c), we we have chosen to plot just a single non-trivial array entry. The reason for this is that the difference between algorithms $\mathcal{R}_3$ and $\mathcal{R}_2$ is only visible on a very small scale; much smaller than the difference in values of the tensors. Analogously, for the volume tensors $\Phi_2^{r,0}(A)$ with $r \in \{0, 1, 2\}$, we plot only the entry corresponding to the area $\Phi_2^{0,0}(A) = \pi$ in Figure 6. The reader should note the precision on the y-axis before concluding that $\mathcal{R}_3$ is significantly poorer than $\mathcal{R}_2$ for volume tensor estimation; from $R_{\max} > 0.0023$, the error of any volume tensor estimator computed by $\mathcal{R}_3$ in this step is below 1%.

The behaviour shown for these selected tensors is representative of the tensors of A. No estimators for tensors that are equal to zero are included in our plots because the estimators likewise equal zero independently of the choices of radii in any step of procedure $\mathcal{P}$ for both algorithms.

From Figure 5(a), representing step (1) of $\mathcal{P}$, we observe that unless the radii are all chosen below 0.02, the choice of radii does not seem to have much effect on

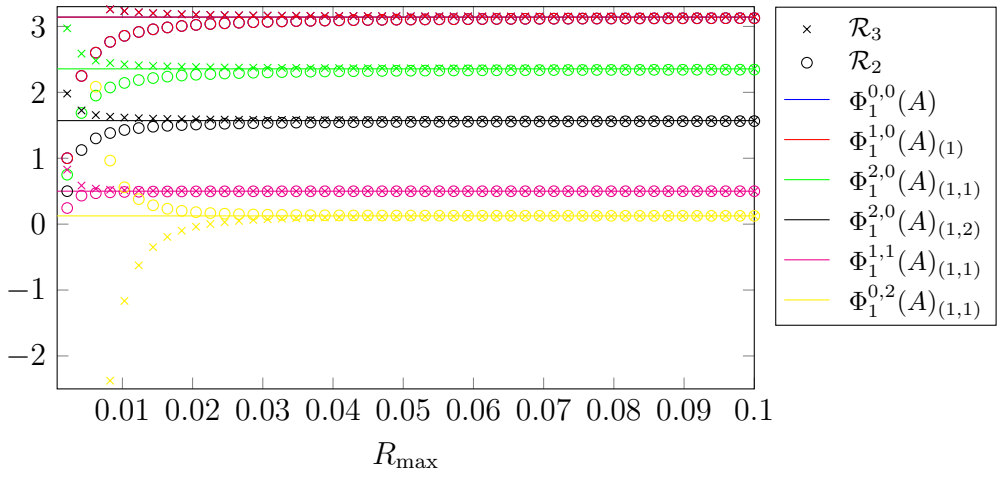

(a) Procedure $\mathcal{P}(1)$ with $R_0 = R_{\max}/n$ for $\mathcal{R}_n$ with $n = 2, 3$.

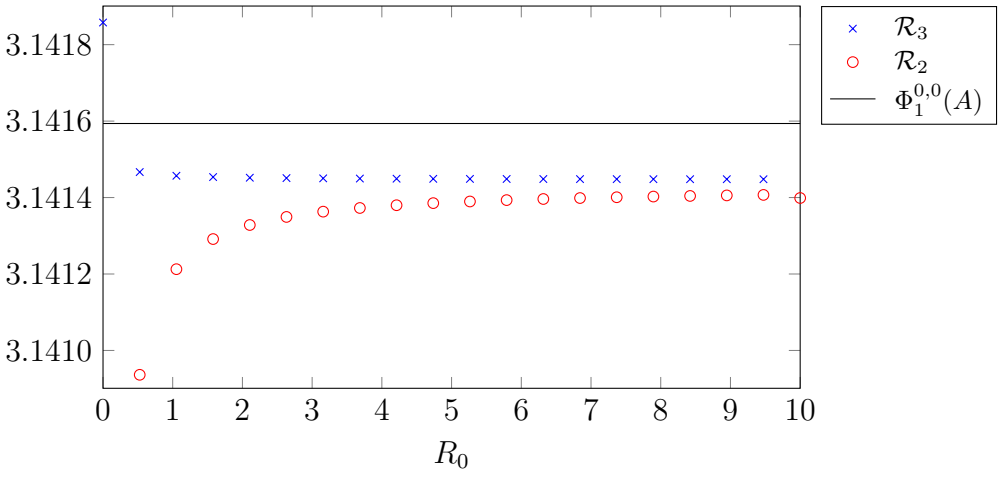

(b) Procedure $\mathcal{P}(2)$ with $R_{\max} = 10$.

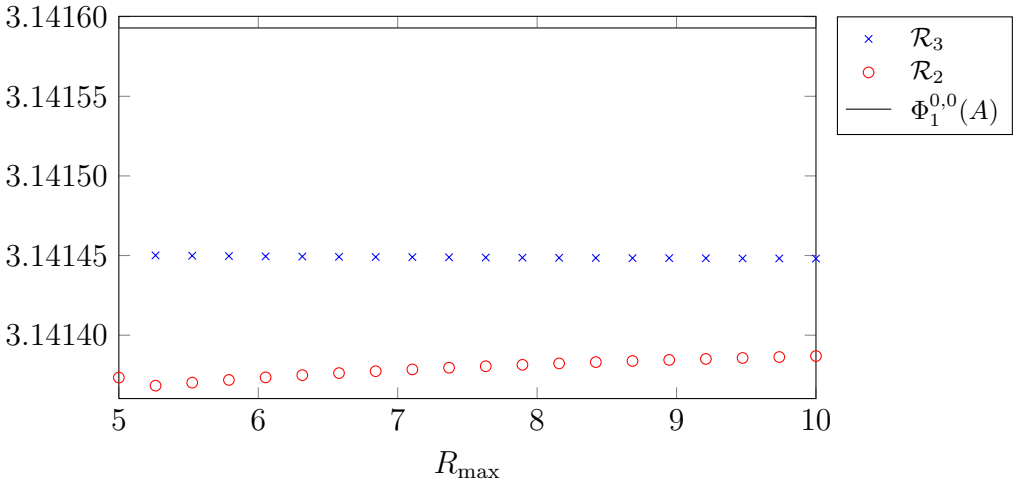

(c) Procedure $\mathcal{P}(3)$ with $R_0 = 5$.

Figure 5: The quality of estimators for the tensors $\Phi_1^{r,s}(A)$, $r, s \geq 0$, $r + s \leq 2$, for fixed resolution $d^{-1} = 1000$ and different radii for the disc $A = B_1 + (1, 1)^T$. The estimators for $\Phi_1^{0,0}(A)$ and $\Phi_1^{1,0}(A)_{(1)}$ overlap completely, thus explaining why $\Phi_1^{0,0}(A)$ does not show in (a).

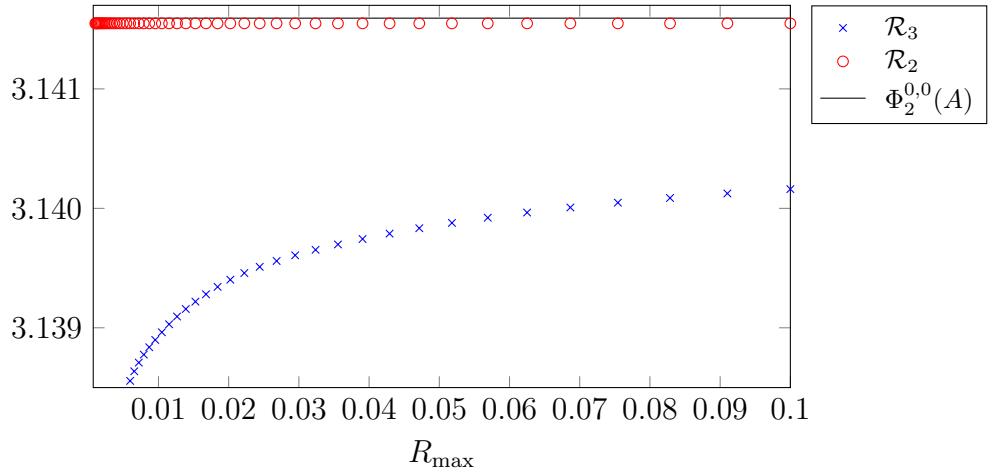

Figure 6: Procedure $\mathcal{P}(1)$ for the disc $A = B_1 + (1,1)^T$ with $d^{-1} = 1000$ and $R_0 = R_{\max}/n$ for $\mathcal{R}_n$ with $n = 2, 3$.

the computed estimators. In the figure, we have zoomed in on the small interval $(d/\sqrt{2}, 0.1]$ to illustrate this point. When $R_{\max}$ is chosen larger than 0.4, the error of the estimators is below 1% for both algorithms. For $\mathcal{R}_3$ in particular, $R_{\max}$ need only be greater than 0.2 to obtain this accuracy. This means that even though we have no upper limit on $R_{\max}$, we need not choose an extremely large value but could select $R_{\max}$ equal to e.g. a few times the diameter of the object. In Figure 5(b), which corresponds to step (2) of procedure $\mathcal{P}$, we examine the algorithms for $R_{\max} = 10$. We observe that problems arise only when R_0 is chosen in the lower half of the interval $(0, 10)$. Indeed, if we choose $R_0 = 0.01$ or 0.1 in step (3), we get large errors for $\mathcal{R}_2$. In comparison, $\mathcal{R}_3$ is less affected by our choice of R_0 and is generally more accurate than $\mathcal{R}_2$. In Figure 5(c), we put $R_0 = 5$ and observe that varying $R_{\max}$ has close to no effect as long as we do not choose it too close to R_0.

There is an apparent tendency in figures 5(b) and (c) of the estimators to converge to some wrong value of the tensor. This, however, is not in conflict with our theoretical expectations. The estimators are expected to converge to the true tensors as we increase the resolution, and in these simulations, we have fixed a resolution and are simply examining the importance of the choices of radii. The examination of the importance of the resolution follows in the next subsection.

From Figure 5(a), we see a tendency of the algorithms to approximate the tensors either from above or below. One could ask whether relations

$$\hat{\Phi}_k^{r,s}(A) \leq \Phi_k^{r,s}(A) \leq \tilde{\Phi}_k^{r,s}(A)$$

exist, possibly with the inequalities reversed depending on the choice of $k, r, s \in \{0, 1, 2\}$, $r + s \leq 2$. However, we see from Figures 5(b) and (c) that this is not the case as both algorithms underestimate the tensor.

Analogously, we now follow procedure $\mathcal{P}$ in the case of a non-convex set. We choose to consider the annulus $A = \mathrm{cl}(B_2 \setminus B_1) + (1,1)^T$. The reach of A is 1, so we must choose $d/\sqrt{2} < R_0 < R_1 < R_2 < 1$. However, we now repeat procedure $\mathcal{P}(1)$ for this non-convex set and allow for radii above the theoretical upper limit $\mathrm{Reach}(A)$ in order to investigate how this affects the estimators. The result is illustrated in

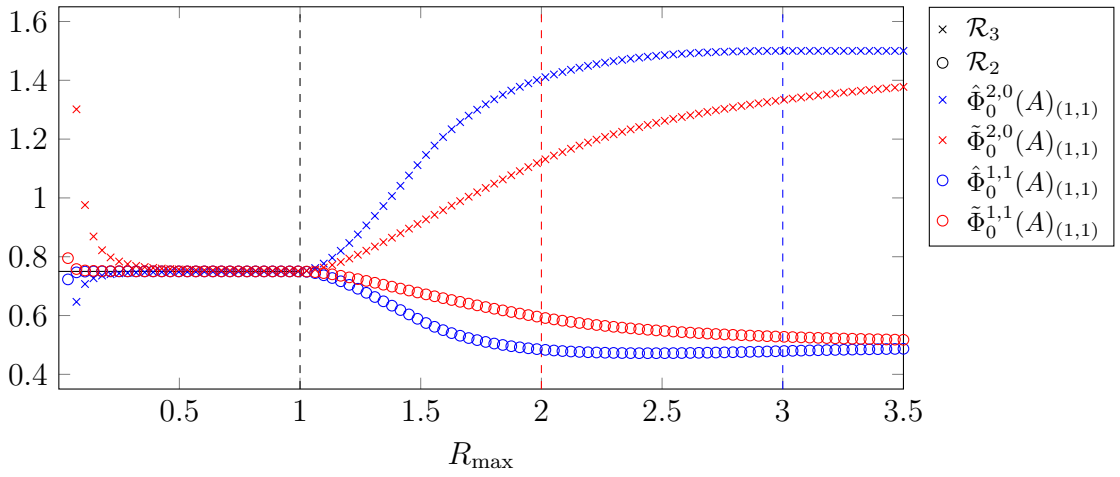

Figure 7: Procedure $\mathcal{P}(1)$ for the annulus $A = \mathrm{cl}(B_2 \setminus B_1) + (1,1)^T$ with $d^{-1} = 1000$ and $R_0 = R_{\max}/n$ for $\mathcal{R}_n$ with $n = 2, 3$. The dashed black line indicates the point when $R_{\max}$ is greater than $\mathrm{Reach}(A)$; the coloured dashed lines when all radii of the corresponding algorithm are above $\mathrm{Reach}(A)$.

Figure 7, where we have chosen to plot the non-zero tensor entries $\Phi_0^{2,0}(A)_{(1,1)}$ and $\Phi_0^{1,1}(A)_{(1,1)}$. Clearly, as soon as $R_{\max} > \mathrm{Reach}(A)$, the estimators become highly unreliable. There is no visible effect when the lower radii also surpass the upper bound.

For radii within the permitted range $(d/\sqrt{2}, \mathrm{Reach}(A))$, we get a picture similar to the one for the disc, but since the radii are now limited to a smaller interval, we see the effect of choosing the radii too close to one another to a greater extent. The picture is similar for the remaining tensors: for $R_{\max}$ greater than 0.25, the error of $\mathcal{R}_3$ is below 1%, whereas we need $R_{\max} > 0.5$ for the same precision in $\mathcal{R}_2$. In general, results improve for higher choices of $R_{\max}$, and with $R_{\max} = 0.95$, we obtain an error below 0.3%. For step (2) of procedure $\mathcal{P}$, we thus pick $R_{\max} = 0.95$. The picture here resembles Figure 7, so we do not include the plot. Again, we need to choose R_0 near the middle of the interval $(d/\sqrt{2}, R_{\max})$ in order to get satisfactory results suggesting a strategy for choosing R_0 when $R_{\max}$ is fixed. This becomes even more apparent when we simulate for fixed R_0 in step $\mathcal{P}(3)$. Indeed for R_0 equal to for instance 0.1, the estimators are rather poor, most prominently for $\mathcal{R}_2$, no matter how we choose $R_{\max}$. Choosing $R_0 = 0.5$ gives much more accurate estimators, in particular if $R_{\max}$ is chosen close to $\mathrm{Reach}(A)$.

It thus appears that a recommendation for non-convex sets is to choose $R_{\max}$ close to the upper limit $\mathrm{Reach}(A)$ and put $R_0 = R_{\max}/2$. These recommendations are at least valid for the non-convex annulus, and it is now natural to ask whether they apply also in the case of other, possibly more complex, non-convex sets.

One candidate for a more complex non-convex set is the complement of a (stationary) Boolean model. We will not go into details with the definition of Boolean models here since we will only consider one concrete example; the interested reader is instead referred to [17, Section 4.3]. Consider a stationary Poisson point process in $\mathbb{R}^2$ with intensity $\gamma > 0$. A random compact set is attached to each point of the process in such a way that the random sets are independent of each other and of

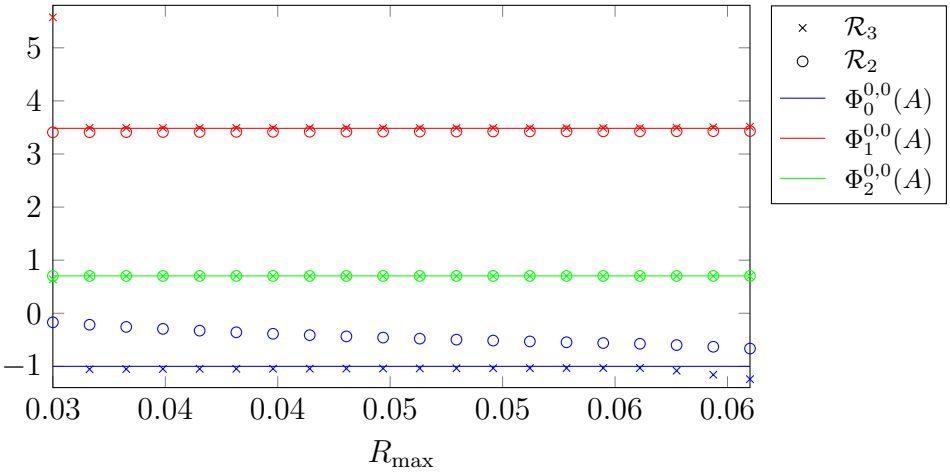

Figure 8: Procedure $\mathcal{P}(3)$ for the complement A of the Boolean model in Figure 4(c) with $d^{-1} = 1000$ and $R_0 = 0.03$.

the Poisson process. The union Z of these sets forms a stationary Boolean model. We consider here a Poisson process with intensity $\gamma = 10$ and discs as random compact sets with a radius distribution given by the uniform distribution $U(a, b)$ in the interval between $a = 0.08$ and $b = 0.16$.

We will analyse Minkowski tensors of the Boolean model in the unit square $W = [0, 1]^2$; see Figure 4(c) for the realisation that was used in the analysis. It is clear that $Z \cap W$ does not in general have positive reach (positive reach is only possible if none of the discs overlap). Therefore, we consider instead its complement $A = (Z \cap W)^C$. We have indicated the distance determining the reach of A in Figure 4(c); $\mathrm{Reach}(A) = 0.0614$. We then perform procedure $\mathcal{P}$ but restrict attention to the tensors of rank zero: the Euler characteristic $\Phi_0^{0,0}(A)$, half the perimeter $\Phi_1^{0,0}(A)$, and the area $\Phi_2^{0,0}(A)$ as illustrated by Figure 8. Here, we show the result of simulations for step (3) of procedure $\mathcal{P}$ with $R_0 = 0.03$, which was found by steps (1) and (2) to be a good choice for the minimal radius. For this particular model, it seems we have a challenge in finding truly good radii for obtaining satisfactory estimators. Especially $\mathcal{R}_2$ is prone to error.

One explanation for the less precise estimators for the complement of the Boolean model might be that we need to consider the model for higher resolutions. It is then relevant to ask whether the same choices of radii are equally good for different choices of resolution. We will explore this question shortly. The procedure $\mathcal{P}$ can be applied to a test set for each of the algorithms $\mathcal{R}_3$ and $\mathcal{R}_2$ in turn in order to find good choices of radii for each of them, but one may also choose to find those radii which yield the best results for both algorithms simultaneously. The latter allows for what could be considered a better basis for comparison of the algorithms later on when we fix the radii and let the resolution vary. Incidentally, for the three test sets above, we have chosen the same radii for $\mathcal{R}_3$ and $\mathcal{R}_2$ in the different steps of procedure $\mathcal{P}$ because the best choices for $\mathcal{R}_2$ work equally well for $\mathcal{R}_3$ (although not necessarily the other way around).

We check now whether our choice of resolution affects the way in which we should choose the radii for a given test set. Consider again the disc $B_1 + (1, 1)^T$. The simulations performed for this set, illustrated by Figure 5, make use of a resolution

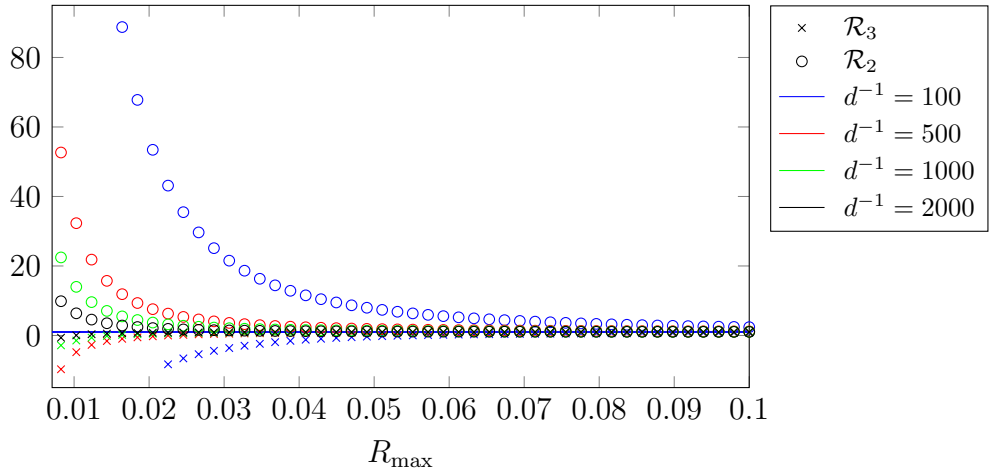

Figure 9: Comparison of effect of choices of radii on estimators for the Euler characteristic, $\Phi_0^{0,0}(A)$, for different choices of resolution in procedure $\mathcal{P}(1)$ for $A = B_1 + (1,1)^T$.

$d^{-1} = 1000$. We now carry out the same simulation but for different resolutions. The results are shown in Figure 9, where the effect is illustrated for the Euler characteristic, $\Phi_0^{0,0}(A)$. The graphs representing each of the four chosen resolutions exhibit a similar behaviour. As could be expected, higher resolution yields better estimators, but from the figure it would seem that the resolution only determines how large radii are needed for good estimators, i.e. for low resolutions, one needs to be able to choose rather high radii whereas high resolutions allow for choices of smaller radii. This tendency is reproducible for the two other test sets as well for all the estimators. This means that if we have a model for which the choice of radii is restricted by the reach, we can compensate by choosing a higher resolution. Moreover, if one choice of radii works well for a given resolution, that same choice will also work for higher resolutions.

As stated in Section 3.3, $\mathcal{R}_3$ sets $R_1 = (R_0 + R_{\max})/2$ by default. We have examined the effect of varying R_1 in the interval $(R_0, R_{\max})$, but except for when R_1 is very close to the limits of the interval, the choice of R_1 seems to have no effect at all. Therefore, minimising the number of input arguments for the algorithm by preassigning R_1 seems the best solution.

Concluding this section, we can give the following general recommendations for the choice of radii. It is advantageous to choose $R_{\max}$ large; we suggest 95% of $\text{Reach}(A)$ in the non-convex case and several diameters of A in the convex case. The smallest radius, R_0, is recommended to be chosen in the middle of the interval $(d/\sqrt{2}, R_{\max})$, which turned out to work well for $\mathcal{R}_2$. Concerning $\mathcal{R}_3$, the choice of R_0 seems less critical as long as it is not chosen too close to either end of the interval $(d/\sqrt{2}, R_{\max})$. For $\mathcal{R}_3$, setting $R_1 = (R_0 + R_{\max})/2$ is recommended, and this choice has already been made in our implementation of the algorithm.

5.2 Influence of resolution on the quality of estimators

Having chosen radii for the three test sets based on procedure $\mathcal{P}$ for a given resolution, we examine the influence of the resolution on the computed estimators; a task which was partly commenced by the comparison in Figure 9. We simulate for

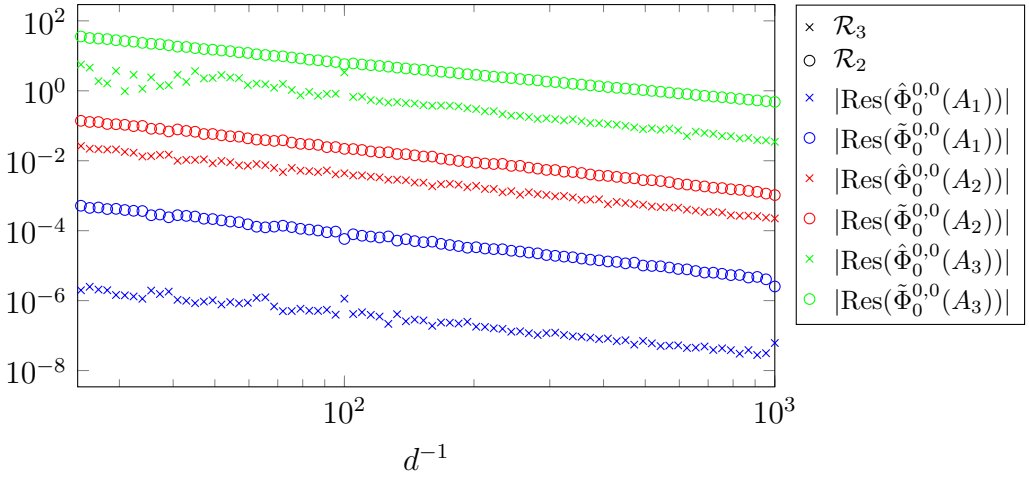

(a) A log-log plot of residuals for the Euler characteristic $\Phi_0^{0,0}(A)$ as functions of the resolution.

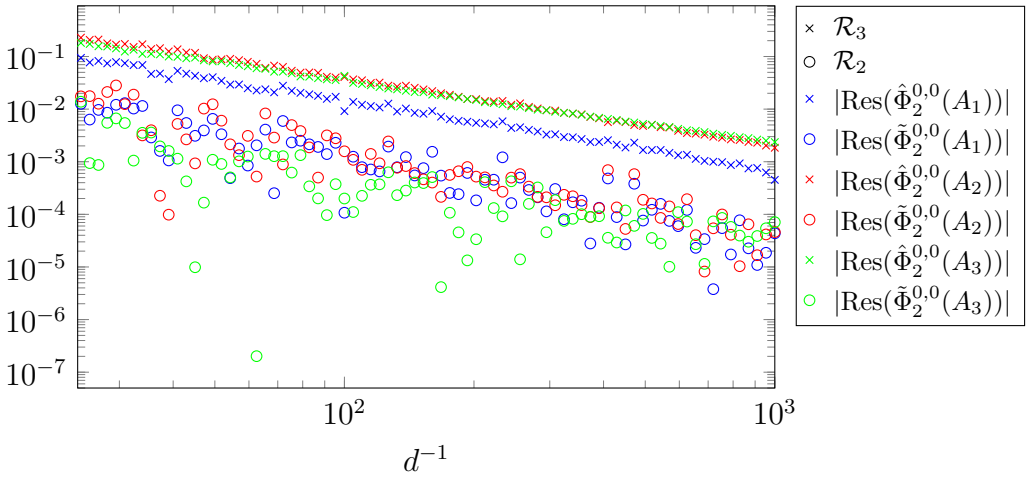

(b) A log-log plot of residuals for the area $\Phi_2^{0,0}(A)$ as functions of the resolution.

Figure 10: Plots of the absolute Minkowski tensor residuals as functions of the resolution for the three test sets $A_1 = B_1 + (1,1)^T$ with $R_0 = 5$, $R_{\max} = 10$; $A_2 = \mathrm{cl}(B_2 \setminus B_1) + (1,1)^T$ with $R_0 = 0.5$, $R_{\max} = 0.95$, and A_3 the complement of the Boolean model with $R_0 = 0.03$, $R_{\max} = 0.05$.

varying choices of resolution and plot the estimators as functions hereof.

Figure 10 shows results for the three test sets of the previous subsection. As we have fixed the radii, we have automatically set a lower limit for the resolution, since we need to make sure that $d/\sqrt{2} < R_0$. As the three sets are plotted together, the set with the smallest R_0, the complement of the Boolean model, determines the minimal resolution. Thus for $R_0 = 0.03$, the resolution should be at least 24.

The functions plotted in Figure 10 are not, as previously, the estimators. Rather, we plot the absolute deviation of the estimator from the true tensor; the absolute residual. The residual $\hat{\Phi}_k^{r,s}(A) - \Phi_k^{r,s}(A)$ of the estimator $\hat{\Phi}_k^{r,s}(A)$ is denoted by $\mathrm{Res}(\hat{\Phi}_k^{r,s}(A))$ for $k, r, s \in \{0,1,2\}$ with $r + s \leq 2$. Figure 10(a) shows the result for the Euler characteristic, $\Phi_0^{0,0}(A)$, and Figure 10(b) that for the area, $\Phi_2^{0,0}(A)$. The functions are plotted on a log-log scale. This way, we are able to check the rate of

convergence. Indeed, summing up on previous remarks, for estimators of the intrinsic volumes, $\Phi_k^{0,0}(A)$ with $k \in \{0,1,2\}$, calculated by either algorithm, the rate of convergence is of order $O(d)$ if A is convex or ρ-regular. In fact, for the volume tensors, $\mathcal{R}_2$ yields estimators that converge to $\Phi_2^{r,0}(A)$ with $r \in \{0,1,2\}$ with speed $O(d)$ if A is a compact topologically regular set with boundary a 1-rectifiable Lebesgue null set, which is less restrictive than the requirements of convexity or ρ-regularity.

That the speed of convergence of the estimator $\hat{\Phi}_k^{r,s}(A)$ towards $\Phi_k^{r,s}(A)$ is $O(d^m)$ for $m \in \mathbb{R}$ means that

$$\mathrm{Res}(\hat{\Phi}_k^{r,s}(A)) \leq c \cdot d^m$$

for some $c \in \mathbb{R}$, where $\hat{\Phi}_k^{r,s}(A)$ is inherently a function of d. This implies that

$$\log|\mathrm{Res}(\hat{\Phi}_k^{r,s}(A))| \leq \log(c) + m\log(d). \tag{5.1}$$

The disc is both convex and ρ-regular for $\rho = 1$, and the annulus is ρ-regular for $\rho = 1$. The complement of the Boolean model is neither, but its boundary is 1-rectifiable. Hence, by (5.1), we expect to see linear graphs in Figures 10(a) and 10(b) with slope m equal to -1 (we are plotting as functions of d^{-1} and not d) for the disc and the annulus. For the complement of the Boolean model we expect the same in Figure 10(b), but we have no theoretical results on its convergence rate for the Euler characteristic.

In Figure 10(a), linear fitting approximations yield:

$$\begin{aligned}
|\mathrm{Res}(\hat{\Phi}_0^{0,0}(A_1))| &\approx 1.19 \cdot \log(d) - 9.15;\\
|\mathrm{Res}(\tilde{\Phi}_0^{0,0}(A_1))| &\approx 1.28 \cdot \log(d) - 3.52;\\
|\mathrm{Res}(\hat{\Phi}_0^{0,0}(A_2))| &\approx 1.27 \cdot \log(d) + 0.36;\\
|\mathrm{Res}(\tilde{\Phi}_0^{0,0}(A_2))| &\approx 1.30 \cdot \log(d) + 2.18;\\
|\mathrm{Res}(\hat{\Phi}_0^{0,0}(A_3))| &\approx 1.69 \cdot \log(d) + 7.86;\\
|\mathrm{Res}(\tilde{\Phi}_0^{0,0}(A_3))| &\approx 1.30 \cdot \log(d) + 8.01.
\end{aligned}$$

These simulations indicate the following conclusions: Firstly, at least for the given example sets, the asymptotic speed of convergence already holds for finite resolution for a range of d that is realistic in practical applications. Even for the Boolean model, for which we do not have an asymptotic speed of convergence bound from theory, the speed is at least linear. Secondly, and maybe even more interestingly, the speed of convergence in the examples is clearly better than d^m with $m = 1$ as suggested by the theory. This indicates that an improved asymptotic convergence rate holds and could possibly be proven, at least for certain subclasses of sets with positive reach.

Similar conclusions can be made for Figure 10(b), where the linear equations are given by:

$$\begin{aligned}
|\mathrm{Res}(\hat{\Phi}_2^{0,0}(A_1))| &\approx 1.30 \cdot \log(d) + 1.72;\\
|\mathrm{Res}(\tilde{\Phi}_2^{0,0}(A_1))| &\approx 1.56 \cdot \log(d) + 0.30;\\
|\mathrm{Res}(\hat{\Phi}_2^{0,0}(A_2))| &\approx 1.28 \cdot \log(d) + 2.66;\\
|\mathrm{Res}(\tilde{\Phi}_2^{0,0}(A_2))| &\approx 1.41 \cdot \log(d) - 0.31;\\
|\mathrm{Res}(\hat{\Phi}_2^{0,0}(A_3))| &\approx 1.42 \cdot \log(d) + 3.41;\\
|\mathrm{Res}(\tilde{\Phi}_2^{0,0}(A_3))| &\approx 1.24 \cdot \log(d) - 2.27.
\end{aligned}$$

Again, the speed of convergence is super-linear in the considered range of d. It appears that the speed of convergence of $\tilde{\Phi}_2^{0,0}(A)$ is better than the one of $\hat{\Phi}_2^{0,0}(A)$ except for the case $A = A_3$, but the slope in this case is supposedly less meaningful due to the huge fluctuation of the residuals (green circles). In fact, the coefficient of determination, R^2, equals 0.59 compared to 0.87 for $A = A_1$ and 0.78 for $A = A_2$, indicating that the regression line is a rather poor approximation in the case $A = A_3$.

That $\tilde{\Phi}_2^{0,0}(A)$ performs particularly well for A_1 and A_2 is explained by the fact that this estimator is based on the basic counting scheme (4.1). For the circle, $A = A_1$, the speed of convergence problem corresponds essentially to the Gauss circle problem, where the best known exponent [9] is $m = 285/208 \approx 1.37$, but it is conjectured [6] to be $m = 1.5 - \varepsilon$ for arbitrary $\varepsilon > 0$.

The graphs for $\mathcal{R}_2$ exhibit strong fluctuations of the residuals. However, as the estimators for the volume tensors, $\tilde{\Phi}_2^{r,0}(A)$ with $r \in \{0, 1, 2\}$, are essentially based on counting sampling points in A as explained above, a so-called Zitterbewegung effect [1, p. 307], known from systematic sampling, occurs here, thus explaining the fluctuations.

The rate of convergence for $\hat{\Phi}_k^{r,s}(A)$ and $\tilde{\Phi}_k^{r,s}(A)$ with $k, r, s \in \{0, 1, 2\}$ and $r+s \in \{1, 2\}$ for convex and ρ-regular sets is $O(\sqrt{d})$. This asymptotic result is also tested in practise for the disc and the annulus in Figure 11. Here, the absolute residual for the tensor $\Phi_1^{1,1}(A)_{(1,1)}$ is plotted. As before, we obtain linear equations:

$$
\begin{aligned}
|\mathrm{Res}(\hat{\Phi}_1^{1,1}(A_1)_{(1,1)})| &\approx 1.30 \cdot \log(d) - 0.13;\\
|\mathrm{Res}(\tilde{\Phi}_1^{1,1}(A_1)_{(1,1)})| &\approx 1.30 \cdot \log(d) - 0.10;\\
|\mathrm{Res}(\hat{\Phi}_1^{1,1}(A_2)_{(1,1)})| &\approx 1.23 \cdot \log(d) + 0.32;\\
|\mathrm{Res}(\tilde{\Phi}_1^{1,1}(A_2)_{(1,1)})| &\approx 1.31 \cdot \log(d) + 1.17,
\end{aligned}
$$

which do not corroborate the theoretically expected rate of convergence corresponding to a slope $m = 0.5$ but rather points to an even higher speed of convergence comparable to that for the intrinsic volumes.

From Figures 10 and 11, it is evident that the more complicated the test set, the higher resolution is required in order for the algorithms to produce good estimators. For the disc, $\mathcal{R}_3$ has en error below 1% for resolutions above $d^{-1} = 46$ compared to $d^{-1} = 80$ for the annulus. For the complement of the Boolean model, we need resolutions well above 2000 to obtain such accurate estimators. In comparison, $\mathcal{R}_2$ has an error below 1% for resolutions above $d^{-1} = 45$ for the disc but $d^{-1} = 285$ for the annulus. We cannot obtain this accuracy for the Boolean model with resolutions below 10 000, but above 9000, we can get below 5%.

The majority of the previous plots have neglected to report results for tensors that are (trivially) equal to zero with the exception of the Euler characteristic of the annulus in Figure 10(a). For completeness, we plot such estimators in Figure 12, again for the annulus. We see that not all estimators are identically zero, and here, too, results depend on the resolution. All zero-tensor estimators are reported by the algorithms $\mathcal{R}_3$ and $\mathcal{R}_2$, so these can be used as indicators of the overall quality of the estimators for a given resolution. The zero-tensors for the disc are in fact identically zero regardless of resolution, confirming that more complicated sets demand higher resolutions.

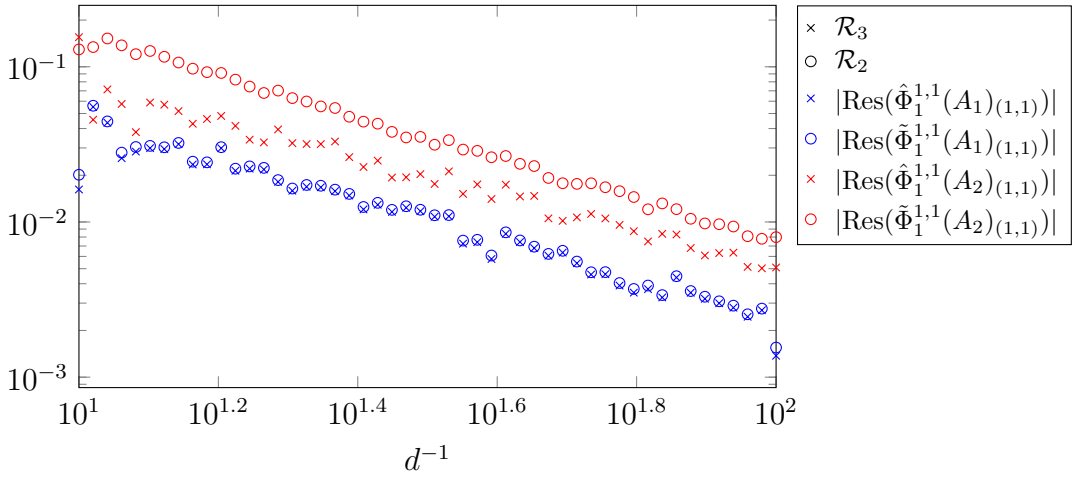

Figure 11: A log-log plot of the absolute Minkowski tensor residuals for a rank two tensor as a function of the resolution for $A_1 = B_1 + (1,1)^T$ with $R_0 = 5$, $R_{\max} = 10$ and $A_2 = \mathrm{cl}(B_2 \setminus B_1) + (1,1)^T$ with $R_0 = 0.5$, $R_{\max} = 0.95$.

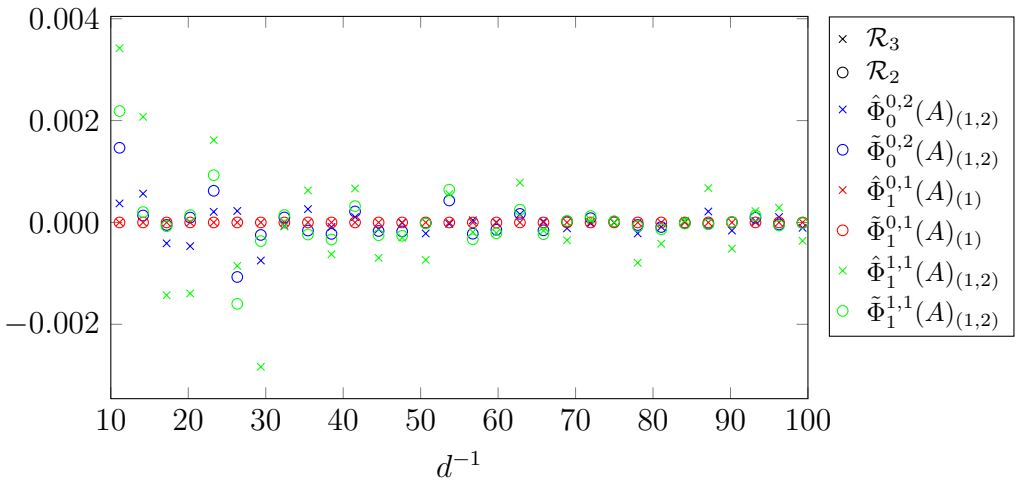

Figure 12: Plot of the Minkowski tensor estimators for zero-tensors as functions of the resolution for $A = \mathrm{cl}(B_2 \setminus B_1) + (1,1)^T$ with $R_0 = 0.5$, $R_{\max} = 0.95$.

From our simulations, we make the following observations. Firstly, it has proven particularly difficult to compute good estimators for the Euler characteristic, $\Phi_0^{0,0}(A)$, for both algorithms $\mathcal{R}_3$ and $\mathcal{R}_2$, unless we consider very simple models such as the disc. Secondly, $\mathcal{R}_2$ produces better estimators for the volume tensors than $\mathcal{R}_3$. Lastly, smaller resolutions suffice for simpler models. This means that for the simplest model, the disc, all tensors are computed fairly accurately by both algorithms already for low resolutions, and residuals of both algorithms are low. In this case, the error of $\mathcal{R}_2$ is smaller than that of $\mathcal{R}_3$ because the volume tensors are the ones more difficult to estimate. However, as complexity of the model increases, difficulty of estimating the Euler characteristic surpasses the volume tensors, and so $\mathcal{R}_3$ becomes the better choice of algorithm since it estimates all but the volume tensors better than $\mathcal{R}_2$.

Regarding the speeds on convergence, the theoretical results for both algorithms already appear to hold under a resolution regime that is realistic in practice. In fact, the speeds of convergence deduced from our simulations are higher than the theoretically expected and also apply to sets that do not meet the necessary requirements for the theorems on multigrid convergence to apply.

Finally, running our simulations in MATLAB, we have observed that $\mathcal{R}_2$ is noticeably faster than $\mathcal{R}_3$. This is likely due to the considerations made at the beginning of Section 5.

6 Discussion

Based on our findings from the various plots in Section 5, we conclude that the algorithms $\mathcal{R}_3$ and $\mathcal{R}_2$ do in fact yield good estimators for the Minkowski tensors in the setting of finite resolution. Algorithm $\mathcal{R}_3$ has proven more accurate than $\mathcal{R}_2$ except in the case of the volume tensors.

On the other hand, $\mathcal{R}_2$ is generally faster than $\mathcal{R}_3$ in computing the estimators, and for sufficiently high resolutions, $\mathcal{R}_2$ does produce satisfactory estimators. Computations times are, however, fairly small in general. Thus, to obtain the best results, our recommendation is to use (4.1) to obtain reliable estimators for the volume tensors and subsequently use $\mathcal{R}_3$ to estimate the remaining Minkowski tensors. Hence we suggest not to use $\mathcal{R}_2$ at all apart from its volume tensor estimators in (4.1). First applying (4.1) and thereupon $\mathcal{R}_3$ increases computation times but yields far better estimators. The algorithm defined in this way is named Minktensor2D:

Algorithm Minktensor2D

Input:

- Digitisation $A_0 = A \cap dL$ of a compact topologically regular set $A \subset \mathbb{R}^2$ with positive reach;
- Lattice distance $d > 0$ of dL;
- Two radii R_0 and R_2 satisfying $d/\sqrt{2} < R_0 < R_2 < \mathrm{Reach}(A)$.

Action:

- Calculate $\hat{\Phi}_2^{r,0}(A_0)$ using (4.1) for $r \in \{0, 1, 2\}$;
- Calculate $\mathcal{V}_{R_i}^{r,s}(A_0)$ using (3.7) for R_i, $i = 0, 1, 2$, with $R_1 = (R_0 + R_2)/2$, and for all $r, s \in \{0, 1, 2\}$ with $r + s \leq 2$;
- Determine the corresponding Minkowski tensors by (3.8).

Output:

- Estimators $\hat{\Phi}_k^{r,s}(A_0)$ for all $k, r, s \in \{0, 1, 2\}$ with $r + s \leq 2$ (including the trivial ones of the form $\hat{\Phi}_k^{0,1}(A_0)$ for model control) of the corresponding Minkowski tensors.

If any result of the algorithm is numerically below 10^{-6}, the output is rounded off to zero.

All MATLAB-files for Minktensor2D are available for download [3].

With regard to the practical use of Minktensor2D, we suggest that in the setting of finite positive reach, one chooses $R_{\max}$ close to but strictly smaller than the reach; for instance $R_{\max}$ equal to 95% of Reach(A). The lower radius R_0 should be chosen near $R_{\max}/2$. When there is no upper bound on $R_{\max}$, i.e. the reach is infinite, $R_{\max}$ can be chosen arbitrarily large, but a choice equal to several diameters of the object is advised. Accuracy of the algorithms is then determined by the resolution. The more complicated the object, the larger resolution is necessary.

A disadvantage of the algorithm is that one needs to know (a lower bound for) the reach of the object. This is a hindrance if one wishes to extract geometric knowledge of some unknown set. Simply guessing the reach can cause major errors, since it is vital that the radii chosen for the algorithm are strictly smaller than the reach as illustrated in Figure 7. Further, in applications, data is not always given as black-and-white digitisations but rather as grey-scale images. Here, one assigns an intensity ranging from 0 to 1 to each sampling point of the lattice depending on the overlap of the object with the Voronoi cell corresponding to the sampling point. Local algorithms for Minkowski tensor estimation based on grey-scale input can for instance be found in [22].

We conclude by mentioning that an implementation of the above algorithms in dimension three or higher is possible. However, it appears to be difficult to determine the integrals on the right-hand side of (3.7) numerically. One possibility would be to use a sufficiently fine approximation of the R-bounded Voronoi cells by polytopes for which an exact evaluation of the corresponding integral is possible. This has already been used in [13] to solve a related problem.

Acknowledgements

The authors were supported by the Centre for Stochastic Geometry and Advanced Bioimaging, funded by the Villum Foundation.

References

[1] Adrian Baddeley and Eva B. Vedel Jensen. *Stereology for statisticians.* CRC Press, 2004.

[2] Claus Beisbart, Marconi S. Barbosa, Herbert Wagner, and Luciano da F. Costa. Extended morphometric analysis of neuronal cells with Minkowski valuations. *The European Physical Journal B-Condensed Matter and Complex Systems*, 52(4):531–46, 2006.

[3] Sabrina Tang Christensen. Minktensor2D. URL `https://gist.github.com/SabrinaGeggie/08634a26664ed7e17344422d42293a6b`.

[4] Sabrina Tang Christensen. *Reconstruction of topology and geometry from digitisations.* PhD thesis, Aarhus University, Ny Munkegade 118, 8000 Aarhus C, Denmark, 2016.

[5] Ulrich Clarenz, Martin Rumpf, and Alexandru Telea. Robust feature detection and local classification for surfaces based on moment analysis. *IEEE Transactions on Visualization and Computer Graphics*, 10(5):516–24, 2004.

[6] Richard Guy. *Unsolved problems in number theory*, volume 1. Springer Science & Business Media, 2013.

[7] Daniel Hug and Rolf Schneider. Local tensor valuations. *Geometric and Functional Analysis*, 24(5):1516–64, 2014.

[8] Daniel Hug, Markus Kiderlen, and Anne Marie Svane. Voronoi-based estimation of Minkowski tensors from finite point samples. *CSGB Research Reports*, (06), April 2016.

[9] Martin N. Huxley. Integer points, exponential sums and the Riemann zeta function. *Number theory for the millennium, II (Urbana, IL, 2000)*, pages 275–90, 2002.

[10] Sebastian C. Kapfer, Walter Mickel, Fabian M. Schaller, Markus Spanner, Christian Goll, Tomoaki Nogawa, Nobuyasu Ito, Klaus Mecke, and Gerd E. Schröder-Turk. Local anisotropy of fluids using Minkowski tensors. *Journal of Statistical Mechanics: Theory and Experiment*, 2010(11):P11010, 2010.

[11] Reinhard Klette and Azriel Rosenfeld. *Digital geometry: Geometric methods for digital picture analysis*. Elsevier, 2004.

[12] MATLAB. *Version 9.0.0.341360, Release 2016a*. The MathWorks, Inc., Natick, Massachusetts, United States.

[13] Quentin Merigot, Maks Ovsjanikov, and Leonidas Guibas. Voronoi-based curvature and feature estimation from point clouds. *Visualization and Computer Graphics, IEEE Transactions on*, 17(6):743–756, 2011.

[14] Joachim Ohser and Frank Mücklich. *Statistical Analysis of Microstructures in Materials Sciences*. Wiley, New York, 2000.

[15] Theo Pavlidis. *Algorithms for graphics and image processing*. Springer-Verlag Berlin – Heidelberg, 1982.

[16] Rolf Schneider. *Convex bodies: The Brunn-Minkowski Theory*. Cambridge University Press, second expanded edition edition, 2014.

[17] Rolf Schneider and Wolfgang Weil. *Stochastic and Integral Geometry*. Springer-Verlag Berlin Heidelberg, 2008.

[18] G.E. Schröder-Turk, W. Mickel, S.C. Kapfer, M.A. Klatt, F.M. Schaller, M.J.F. Hoffmann, N. Kleppmann, P. Armstrong, A. Inayat, D. Hug, et al. Minkowski tensor shape analysis of cellular, granular and porous structures. *Advanced Materials*, 23 (22-23):2535–53, 2011.

[19] Gerd E. Schröder-Turk, Walter Mickel, Matthias Schröter, Gary W. Delaney, Mohammad Saadatfar, Tim J. Senden, Klaus Mecke, and Tomaso Aste. Disordered spherical bead packs are anisotropic. *EPL (Europhysics Letters)*, 90(3):34001, 2010.

[20] Jean Serra. *Image analysis and mathematical morphology*, volume 1. Academic Press, Inc., 1982.

[21] Peer Stelldinger and Ullrich Köthe. Towards a general sampling theory for shape preservation. *Image and Vision Computing*, 23(2):237–48, 2005.

[22] Anne Marie Svane. Estimation of Minkowski tensors from digital grey-scale images. *Image Anal. Stereol.*, 34:51–61, 2015.

[23] Martina Zähle. Integral and current representation of Federer's curvature measures. *Archiv der Mathematik*, 46(6):557–567, 1986.